JOURNAL OF GEOPHYSICAL RESEARCH
Oceans
AN AGU JOURNAL

JGR

Volume 120 • Issue 2 • February 2015 • Pages 597–1428

AGU PUBLICATIONS

WILEY

AGU PUBLICATIONS

JGR

Journal of Geophysical Research: Oceans

RESEARCH ARTICLE

10.1002/2014JC010267

Tidal bore dynamics in funnel-shaped estuaries

P. Bonneton[1], N. Bonneton[1], J.-P. Parisot[1], and B. Castelle[1]

[1]CNRS, UMR EPOC, University of Bordeaux, Talence, France

Key Points:
- First long-term field characterization of tidal bore formation in estuaries
- Tidal bore intensity is mainly governed by the dimensionless local tidal range
- Identification of a transition for the tidal bore secondary wavefield

Correspondence to:
P. Bonneton,
p.bonneton@epoc.u-bordeaux1.fr

Citation:
Bonneton, P., N. Bonneton, J.-P. Parisot, and B. Castelle (2015), Tidal bore dynamics in funnel-shaped estuaries, *J. Geophys. Res. Oceans*, *120*, doi:10.1002/2014JC010267.

Received 27 JUN 2014
Accepted 6 JAN 2015
Accepted article online 9 JAN 2015

Abstract The formation and dynamics of tidal bores in funnel-shaped estuaries is investigated from both a global tidal wave scaling analysis and new quantitative field observations. We show that tidal bore occurrence in convergent estuaries can be estimated from a dimensionless scaling parameter characterizing the relative intensity of nonlinear friction versus local inertia in the momentum equation. A detailed analysis of tidal bore formation and secondary wave structure is presented from a unique long-term database (observations of more than 200 tides) acquired during four campaigns in the two main French tidal-bore estuaries: the Seine and Gironde/Garonne estuaries. We describe the effect of freshwater discharge on the global tidal wave transformation at the estuarine scale and on local tidal bore occurrence in the upper estuary. Our field data suggest that the tidal bore intensity is mainly governed by the dimensionless tidal range, which characterizes the local tidal wave nonlinearity. We also show that the secondary wavefield associated with tidal bore propagating in natural estuaries differs significantly from those associated to undular bores in rectangular channels. In particular, we observe an abrupt decrease of the whelp steepness when the Froude number goes below 1.1. This secondary field transition can explain why tidal bore occurrence in worldwide estuaries is certainly underestimated.

1. Introduction

The formation and dynamics of tidal bores in estuaries are highly complex phenomena which bring into play nonlinear interactions over a large range of spatiotemporal scales. Spectacular and fascinating bores, which can form at the leading edge of flood tides, are small-scale estuarine processes with scales of variation of order few seconds in time and dozen meters in space. This small-scale process, which generally occurs in the upper estuary, results from the nonlinear transformation of the tidal wave over long distance (several dozen of kilometers) and long period of time (several hours). The general bore phenomenon has been extensively studied in fluid mechanics and mathematics. On the other hand, the large-scale mechanisms which control tidal bore formation in convergent estuaries has so far received little attention.

A bore is a hydraulic jump in translation. It arises at the transition between two streams with different flow depths. This small-scale phenomenon is not specific to tide environments and can be associated with the transformation of other long wave phenomena, such as tsunami waves [e.g., *Madsen et al*., 2008; *Tissier et al*., 2011]. Bore dynamics has been extensively studied from laboratory experiments [e.g., *Favre*, 1935; *Treske*, 1994; *Soares Frazao and Zech*, 2002; *Chanson*, 2009], theoretical [e.g., *Lemoine*, 1948; *Benjamin and Lighthill*, 1954; *El et al*., 2006] and numerical approaches [e.g., *Peregrine*, 1966; *Wei et al*., 1995; *Soares Frazao and Zech*, 2002; *Tissier et al*., 2011]. Up until the beginning of the 21st century, tidal bore description in natural environments was essentially based on qualitative observations [e.g., *Lynch*, 1982; *Bartsch-Winkler and Lynch*, 1988]. However, in the last 10 years, several quantitative field studies have contributed to a better understanding of wave, turbulent, and sediment processes associated with tidal bore propagation up river [*Simpson et al*., 2004; *Wolanski et al*., 2004; *Uncles et al*., 2006; *Bonneton et al*., 2011a, 2012; *Chanson et al*., 2011; *Furgerot et al*., 2013]. Most of these studies focus on small-scale bore processes and are based on short-time campaigns encompassing a limited range of freshwater discharge and tidal wave conditions.

The objective of the present study is to analyze tidal bore formation and dynamics in funnel-shaped estuaries as a whole, from large-scale tidal wave transformation to small-scale wave processes associated with tidal bores. This analysis relies on several long-term campaigns on the two main French tidal-bore estuaries: the Gironde/Garonne and the Seine estuaries. Estuarine flows were measured for several neap-spring tide cycles and for contrasting water discharges (observations for more than 200 tides). Preliminary results from

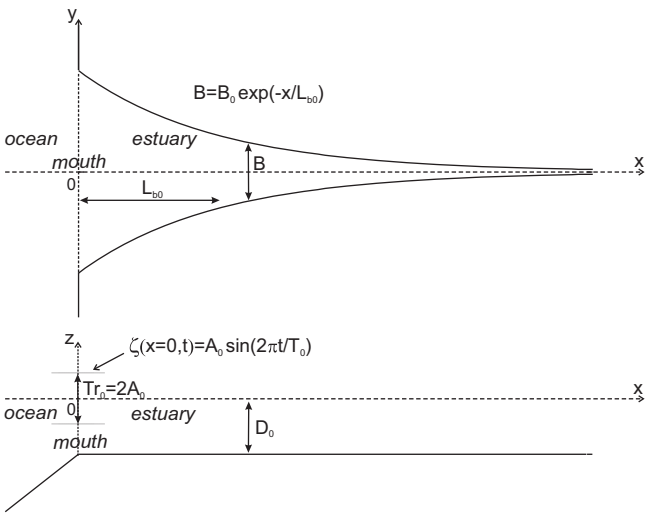

Figure 1. Sketch of a convergent estuary. $B(x)$, channel width; L_{b0}, convergence length; D_0, characteristic water depth; $Tr_0 = 2A_0$, tidal range at the estuary mouth; T_0, tidal period; and ζ, surface elevation.

these observations have already been published. They were focused on tidal bore occurrence [*Bonneton et al*., 2012] and large amplitude tidal bore characteristics [*Bonneton et al*., 2011b]. In the present paper, we go further by investigating the effects of freshwater discharge on both the tidal wave transformation at the global estuary scale and the bore formation in the upper estuary at a local scale. We also analyze in detail the properties of the secondary wavefield associated with undular tidal bores.

Section 2 presents an overview of tidal bore dynamics, ranging from large to small scales. This overview is based on both a review of the current literature and some new materials. Most specifically, we will discuss in detail the conditions favorable to tidal bore occurrence in funnel-shaped estuaries, from a scaling analysis of the global tidal wave transformation in terms of tidal forcing at the estuary mouth and large-scale geometrical properties of the channel. Long-term field experiments on the Gironde/Garonne and Seine estuaries are described in section 3, then the analysis of these field data, from large to small scales, is discussed in section 4.

2. Physical Background

An overview of tidal bore dynamics, from large (section 2.1) to small scales (section 2.3) is presented in this section. This presentation also highlights open scientific issues which will be investigated in section 4.

2.1. Scaling Analysis

Tidal bore formation results from the nonlinear distortion of a tidal wave propagating upstream a convergent estuary. The quantitative analysis of this physical process and the determination of the conditions under which bores form in an estuary are still an open issue. However, simple bore formation criteria can be found in the literature [e.g., *Bartsch-Winkler and Lynch*, 1988; *Chanson*, 2012]. For instance, in his numerous publications, *Chanson* asserts that *a tidal bore forms when the tidal range exceeds 4–6 m and the flood tide is confined to a narrow funneled estuary*. Even if the tidal range is a key parameter for tidal bore formation, we will show in this paper that such simple criteria are not relevant to determine tidal bore occurrence (see section 4.1). Tidal bore formation not only depends on incoming tide amplitude, but also on tidal wave transformation up the estuary, which is largely controlled by a competition between bottom friction, channel convergence, and freshwater discharge [e.g., *Friedrichs*, 2010; *Savenije*, 2005]. If little is known about tidal bore formation, conversely the analysis of tidal wave transformation in convergent estuaries, in terms of tidal forcing at the estuary mouth and large-scale geometrical properties of the channel, has already received considerable attention [e.g., *LeBlond*, 1978; *Parker*, 1991; *Friedrichs and Aubrey*, 1994; *Lanzoni and Seminara*, 1998; *Toffolon et al*., 2006; *Savenije et al*., 2008]. In this section, we will follow the scaling analysis developed in these studies to shed light on the conditions favorable to tidal bore occurrence.

In order to reduce the number of parameters of this problem (see Table 1), we consider a schematic channel geometry (see Figure 1). Most convergent estuaries are shaped with a width that tapers upstream in an approximately exponential fashion and with a fairly horizontal bottom [see *Lanzoni and Seminara*, 1998; *Davies and Woodroffe*, 2010; *Savenije*, 2005]. The two main characteristic channel length scales are therefore the mean water depth D_0 and the convergence length L_{b0}, which is defined by $L_{b0} = |B/\frac{dB}{dx}|$, where $B(x)$ is the channel width and x is the along-channel coordinate. The forcing tidal wave at the estuary mouth can be characterized by its angular frequency ω_0 and its amplitude $A_0 = Tr_0/2$, where Tr_0 is the estuary mouth tidal

Table 1. Table of Parameters

Parameter	Description
D_0	Characteristic water depth
T_0	Tidal period
$\omega_0 = 2\pi/T_0$	Tidal angular frequency
L_{b0}	Convergence length
Tr_0	Tidal range at the mouth
$A_0 = Tr_0/2$	Tidal amplitude at the mouth
Q_0	Freshwater discharge
U_0	Characteristic tidal velocity
C_{f0}	Characteristic friction coefficient
B	Channel width
x_b	Position of tidal inception
D	Cross-sectional averaged water depth
D_1	Low-tide water depth
ζ	Surface elevation
Tr	Local tidal range
u	Cross-sectional averaged velocity
c_b	Bore celerity
A_w	Secondary wave amplitude
T_w	Secondary wave period
λ_w	Secondary wave wavelength
α_m	Maximum elevation slope of the bore
D_i	Dissipative parameter
D_i^*	Estimate of the dissipative parameter
K	Convergence parameter
$\varepsilon = Tr/D_1$	Local tidal wave nonlinear parameter
Fr	Bore Froude number
$\mu = 2\pi D_1/\lambda_w$	Shallowness parameter

range. Similar to the large majority of tidal bores observed worldwide [*Bartsch-Winkler and Lynch*, 1988], those analyzed in this paper are generated by semidiurnal tides. The characteristic tidal period $T_0 = 2\pi/\omega_0$ is therefore a constant value of 12.4 h. In a tidal bore context, it is apposite to choose the maximum spring tide amplitude at the estuary mouth as the characteristic amplitude A_0. Another important parameter which controls tide propagation in the estuary is the mean friction coefficient C_{f0} [e.g., *LeBlond*, 1978; *Parker*, 1991; *Friedrichs and Aubrey*, 1994; *Lanzoni and Seminara*, 1998]. In order to reduce the complexity of this problem here, we consider that the freshwater discharge, Q_0, can be neglected. We will analyze later, in section 4.1, the effects of freshwater discharge on tidal bore formation.

From a scaling analysis of the nonlinear shallow water equations (Saint Venant equations), we can show (see Appendix A) that the global tidal dynamics is governed by three dimensionless parameters constructed from the external variables of this problem: $\epsilon_0 = \frac{A_0}{D_0}$, $\delta_0 = \frac{(gD_0)^{1/2}\omega_0^{-1}}{L_{b0}}$ and $\gamma_0 = \frac{C_{f0}A_0L_{b0}}{D_0^2}$. *Lanzoni and Seminara* [1998] showed that a classification of the main tidal wave regimes can be based on only two dimensionless parameters: $\mathcal{D}_i$, the relative intensity of friction versus local inertia in the momentum equation and K which measures the kinetic effect of channel convergence relative to the effect of temporal oscillations of the free surface. These parameters are given by the relations:

$$K = \frac{U_0 D_0}{A_0 \omega_0 L_{b0}}, \tag{1}$$

$$\mathcal{D}_i = C_{f0}\frac{U_0}{D_0\omega_0}, \tag{2}$$

where U_0 is the characteristic amplitude of tidal velocity, which can be expressed as a function of the external scales (see *Toffolon et al*. [2006] and Appendix A). *Lanzoni and Seminara* [1998] showed that in weakly dissipative estuaries (i.e., small $\mathcal{D}_i$), tide propagation is a weakly nonlinear phenomenon. Additionally, in strongly dissipative estuaries (i.e., large $\mathcal{D}_i$), tide propagation becomes a strongly nonlinear phenomenon that displays peaking and sharp distortion of the current profile, systematically leading to flood dominance. These last tidal wave characteristics correspond to necessary conditions for tidal bore formation. Many tidal-bore estuaries are characterized by a convergence parameter close to 1 (see Table 2). In this case, the dissipative parameter $\mathcal{D}_i$ can be expressed in an approximate form (see Appendix A) as a function of the external scales:

$$\mathcal{D}_i^* = C_{f0}\frac{A_0 L_{b0}}{D_0^2}. \tag{3}$$

The $\mathcal{D}_i^*$ parameter, which characterizes the intensity of tidal wave nonlinearity, is enhanced for increasing tidal range, friction coefficient and convergence length and decreasing water depth. When this parameter is large, the funnel-shaped estuaries are strongly dissipative and the conditions are favorable to tidal bore formation.

2.2. Tidal Bore Formation

The formation of tidal bores in funnel-shaped estuaries is governed by the progressive distortion of the whole tidal wave as it propagates up the estuary. When the flood-dominated asymmetry is strong enough, generally in the upper estuary, tidal bore can form. The tidal wave distortion process is well illustrated in

Table 2. Geometric and Tidal Properties of Six Tidal Bore Funnel-Shaped Estuaries and Corresponding Values of Dimensionless Parameters: K, $\mathcal{D}_i$, and $\mathcal{D}_i^*$ (Defined by Equations (1)–(3))[a]

	Estuaries	D_0 (m)	L_{b0} (km)	Tr_0 (m)	C_{f0}	U_0 (m/s)	x_b (km)	K	$\mathcal{D}_i$	$\mathcal{D}_i^*$
1	Gironde/Garonne	10	43	5.0	0.0025	1.6	90	1.1	2.8	2.7
2	Hooghly	6	25	4.5	0.0015	1.2*	60	0.90	2.1	2.3
3	Humber	12	25	6.4	0.003	1.0*	75	1.0	1.7	1.7
4	Pungue	4	17	7.0	0.003	1.4*	50	0.67	7.5	11.1
5	Qiantang	10	40	6.5	0.0015	2.0	90	1.1	2.1	2.0
6	Severn	15	41	7.5	0.0025	1.5	55	1.0	1.8	1.7

[a] D_0, water depth; L_{b0}, convergence length; Tr_0, tidal range at the estuary mouth; C_{f0}, friction coefficient; U_0, characteristic velocity; x_b, distance between the estuary mouth and the tidal bore inception. Sources: 1, own data; 2, *Chugh* [1961] and *van Rijn* [2011]; 3, *Uncles et al.* [2006] and *Vandenbruwaene et al.* [2013]; 4, *Graas and Savenije* [2008] and *Cai et al.* [2012]; 5, *Pan and Lu* [2011] and *Zhang et al.* [2012]; 6, *Lanzoni and Seminara* [1998]. *U_0 values estimated from equation (28) of *Toffolon et al.* [2006].

Figure 2, which presents time series of tide elevation in different locations of the Gironde/Garonne estuary (Figure 6) for a large amplitude equinox spring tide. The tidal wave at the estuary mouth is fairly symmetric. As the tide propagates upstream, the wave is deformed and a marked ebb-flood asymmetry develops in the central estuary and subsequently intensifies in the upper estuary (Garonne River) up to Podensac at 125 km from the estuary mouth. At that point, the duration of level rising and level falling are, respectively, 3 h 20 min and 9 h. In parallel, the tidal range, Tr, increases from 5.0 m at the estuary mouth to a maximum value of 6.3 m at Podensac and then decreases further upstream. In the lower and middle estuaries, the beginning of the flood is characterized by a continuous and progressive increase in water elevation. On the other hand, in the upper estuary, the start of the flood is characterized by an inflexion point associated with a water elevation jump (see Figure 3). In Bordeaux (Figure 3a), this jump is weak (around 0.65 m) and settles in 150 s. This phenomenon can be considered as the premise of the tidal bore formation. Further upstream in Podensac (Figure 3b), a strong undular tidal bore is formed. The first wave front is associated with a water elevation increase of 1.25 m in less than 3 s. After Podensac, tidal wave amplitude and asymmetry decrease leading to a decreasing bore intensity and finally to the tidal bore vanishing.

This description of bore formation in the Gironde-Garonne estuary is representative of what occurs in most of the tidal-bore funnel-shaped estuaries. However, if tidal bores occur predominantly in hypersynchronous estuaries (estuaries where convergence overcomes friction and consequently tidal waves are amplified), such as Gironde/Garonne or Hooglhly estuaries, they can also occur in hyposynchronous estuaries (damped tidal wave) such as the Pungue and Seine estuaries. It is important to note that tidal bore formation is a gradual physical process associated with the tidal wave transformation over a long distance, even if local bathymetric changes can also induce significant bore intensity variations. The first step toward tidal bore formation in dissipative funnel-shaped estuaries is the nonlinear transformation of the tidal wave in the lower and middle estuary, which leads to a mark ebb-flood asymmetry. A small undular jump can form at the leading edge of the incoming tide as the tidal wave continues to propagate up the estuary. Table 2 presents the distance, x_b, between the estuary mouth and the position of tidal bore inception for six estuaries. We can see that the tidal bore is not observed in the first 50 km of these estuaries, and only forms at 90 km for the Gironde-Garonne estuary and 100 km for the Seine estuary (not shown in the table). As the tidal wave propagates upstream in the upper estuary, the tidal bore intensity can increase and

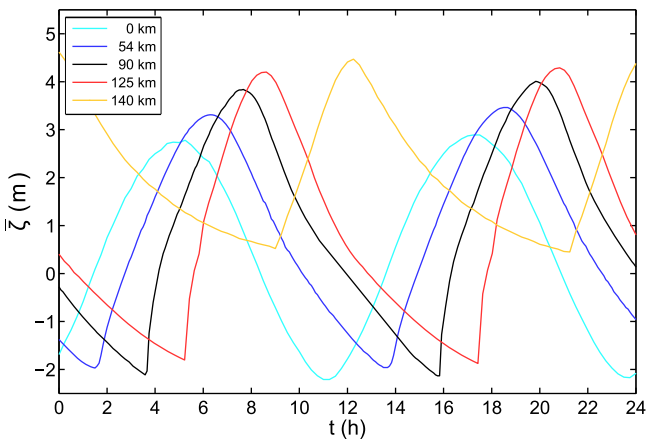

Figure 2. Time series of tide elevation (altimetry NGF-IGN69 system), 10 September 2010 in different locations of the Gironde/Garonne estuary. x = 0 km: estuary mouth (Le Verdon); x = 54 km: middle estuary (Pauillac); x = 90 km: upper estuary (Bordeaux); x = 125 km: upper estuary (Podensac); and x = 140 km: upper estuary (Langon).

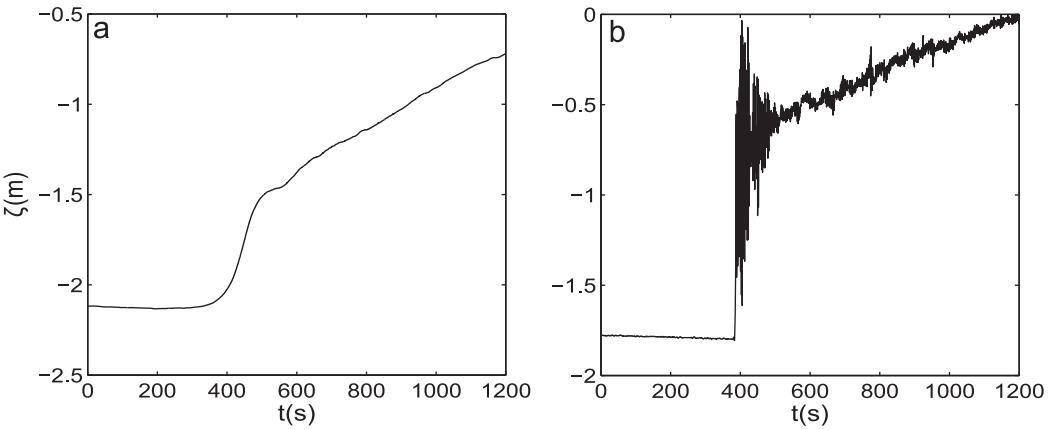

Figure 3. Time series of water surface elevation (altimetry NGF-IGN69 system) in the Garonne River on 10 September 2010, when the tide flow turns to rising. (a) 90 km from the estuary mouth (Bordeaux); (b) 125 km from the estuary mouth (Podensac).

lead to partially breaking undular bores like in the Gironde/Garonne estuary [*Bonneton et al*., 2011a] or even to fully turbulent bores, like in the Qiantang estuary [*Pan and Lu*, 2011]. It is important to emphasize that this spatially graded mechanism is significantly different from the one generally used to generate undular or turbulent bores in laboratory experiments [e.g., *Favre*, 1935; *Treske*, 1994; *Chanson*, 2009], where the bore is abruptly generated by a fast-closing gate at the upstream end of the flume.

The formation of a tidal bore, and especially the location of the onset, is difficult to characterize because it would require a high density of water elevation measurements over a long distance. On the other hand, one can more easily characterize, at a fixed point in space, the time evolution of tidal wave and bore occurrence for varying successive incoming tides [*Bonneton et al*., 2011a, 2012]. This evolution is illustrated in Figure 4 for the Garonne River at the location where tidal waves reach their maximum amplitude. We can observe the progressive transition between a tidal wave regime without bore (Figure 4a), for small tidal range at the estuary mouth Tr_0, and a well-developed undular tidal bore regime for $Tr_0 > 3.4$m (Figures 4h and 4i). For intermediate Tr_0, we can see the appearance of an inflexion point at the beginning of the rising tide and then the formation of a very low intensity undular bore (Figures 4f and 4g).

If tidal wave propagation in the lower and middle estuary is well described by the Saint Venant equations with friction [e.g., *Savenije*, 2005], conversely the onset of the tidal bore and its evolution upstream require the use of other long wave modeling approaches. As shown by *Peregrine* [1966], the undular bore formation is controlled by nonhydrostatic dispersive mechanisms. The onset of the tidal bore can be well described by classical weakly dispersive weakly nonlinear Boussinesq-type equations [*Peregrine*, 1966], but the subsequent nonlinear evolution, for high-intensity tidal bores, requires the use of the basic fully nonlinear Boussinesq equations, named Serre-Green Naghdi equations [*Serre*, 1953; *Green and Naghdi*, 1976; *El et al*., 2006; *Bonneton et al*., 2011c; *Tissier et al*., 2011]. However, *Madsen et al*. [2005] and *Pan and Lu* [2011] used the nondispersive Saint Venant equations with shock capturing numerical methods to simulate the propagation of breaking bores in the Qiantang River. If this approach can not accurately simulate the tidal bore inception, which is a nonhydrostatic process, it gives relatively good results to describe breaking bore propagation [*Pan and Lu*, 2011].

2.3. Undular Bore Characteristics

It is important to describe undular bore characteristics because a large majority of tidal bores in estuaries are of the undular type [*Chanson*, 2012] and, as explained in the previous section, it is also a transition state at the inception of turbulent breaking tidal bore formation. An undular bore is made up of a primary wave, i.e., a mean jump, between two different states of velocity and water depth, on which is superimposed secondary waves, which are named whelps when referred to tidal bores [*Lynch*, 1982; *Bartsch-Winkler and Lynch*, 1988]. This oscillatory wave structure is also frequently called a *dispersive shock wave* in mathematics and physics. Figure 5 shows a representative example of undular tidal bore in a natural estuary. To keep things simple, most of theoretical and laboratory studies have considered bores as the transition between two different uniform flows of water [*Peregrine*, 1966]. It is worthwhile to note that the right state of a tidal bore (see Figures 3–5) does not correspond to a uniform flow, but to the progressive increase of the water

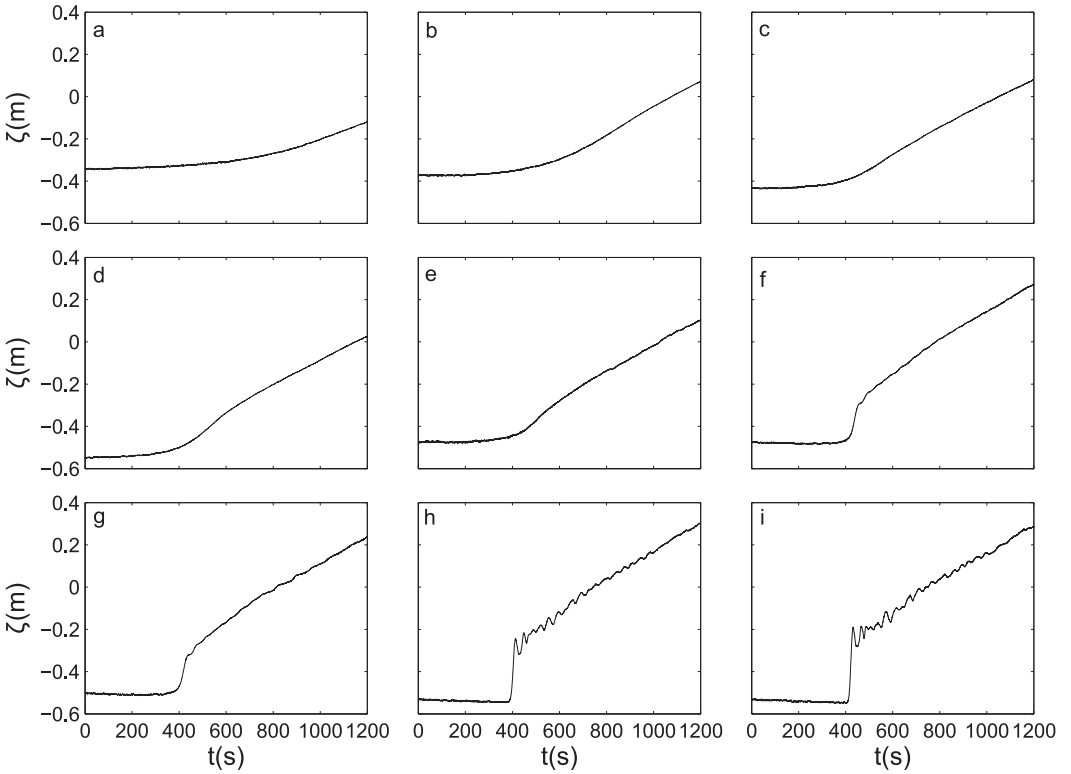

Figure 4. Time-evolution of water surface elevation (altimetry NGF-IGN69 system) at Podensac (Gironde/Garonne estuary) when the tide flow turns to rising. Successive tides from the 10–14 March 2010, for moderately high freshwater discharges (550 m^3/s). (a) $Tr_0 = 1.81$ m; (b) $Tr_0 = 2.07$ m; (c) $Tr_0 = 2.28$ m; (d) $Tr_0 = 2.58$ m; (e) $Tr_0 = 2.75$ m; (f) $Tr_0 = 3.05$ m; (g) $Tr_0 = 3.14$ m; (h) $Tr_0 = 3.43$ m; and (i) $Tr_0 = 3.46$ m.

depth with the rising tide. Another important characteristic of tidal bore propagating in natural estuaries is the strong variability along the estuary cross section of the secondary wavefield, with whelp amplitude generally larger on the banks than on the midchannel [*Bonneton et al*., 2011a, 2011b]. This variability is due to the interaction between the secondary wavefield and the gently sloping alluvial river banks (bank slopes around 0.1–0.3). However, *Bonneton et al*. [2011b, 2012] showed that the mean jump, over which secondary waves propagate, is nearly uniform over the cross section, in agreement with laboratory observations by *Treske* [1994] for bore propagating over a trapezoidal channel.

In this paper, we will analyze the evolution of the mean tidal bore characteristics as a function of both evolving tidal range at the estuary mouth and freshwater discharge. The main tidal bore variables are defined in Figure 5, where $\overline{\zeta}$ is the elevation of the primary wave, $D=D(\overline{\zeta})$ the cross-sectionally averaged water depth and u the cross-sectionally averaged velocity. Positive u-velocities indicate upstream flowing currents. Subscripts 1 and 2 indicate values, respectively, ahead and behind the mean jump. Subscript 1 corresponds also to flow variables at low tide. The mean bore intensity can be characterized by the Froude number $Fr=\frac{|u_1-c_b|}{(gD1)^{1/2}}$, where c_b is the bore celerity.

If undular tidal bores in real estuaries have received little attention, then in contrast, since the pioneer experimental work of *Favre* [1935], the dynamics of undular bores occurring between two uniform flows of water has been extensively studied. For nonbreaking undular bores, the energy loss at the wave front is mainly due to upstream energy radiation through the stationary secondary wavefield. This was shown by *Lemoine* [1948], using linear wave theory and by *Benjamin and Lighthill* [1954] using cnoidal wave theory. However, a detailed description of undular bore formation and dynamics requires a more general modeling framework taking into account their nonstationary dispersive and nonlinear properties. It is now recognized that the Serre or Green Naghdi equations represent the relevant system to model these highly nonlinear weakly dispersive waves [*Lannes and Bonneton*, 2009]. *Wei et al*. [1995] and *Tissier et al*. [2011] simulated with these equations the dynamics of undular bores and obtained good results in comparison with respectively numerical simulations of the Euler equations and laboratory experiments. It is out of the scope of this paper to compare our field data with such a complex modeling approach.

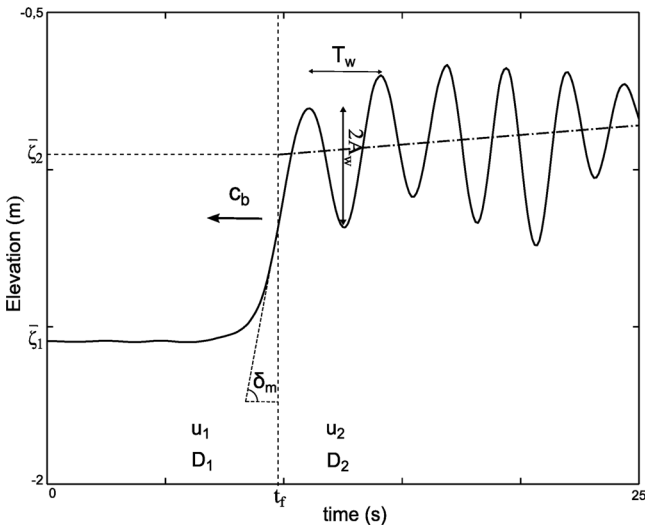

Figure 5. Illustration of undular tidal bore elevation profile in a natural estuary (Garonne River, September 2011) and definition of the characteristic variables. Subscripts 1 and 2 indicate values, respectively, ahead and behind the mean jump (i.e., primary wave). c_b is the bore celerity, $\bar{\zeta}$ the elevation of the mean jump, u the cross-sectionally averaged velocity, and D the cross-sectionally averaged water depth; t_f, time of wave front passage; δ_m, maximum value of the elevation velocity, $\frac{d\zeta}{dt}$, at the wave front; A_w and T_w, amplitude and period of the first whelp (i.e., first secondary wave).

On the other hand, the elegant Lemoine's theory can provide us a very simple and useful tool for analyzing our field results. *Lemoine* [1948] combined the nondispersive shock-wave approach for the primary wave (i.e., the mean bore), with a description of the secondary wavefield based on the monochromatic linear wave theory. He obtained simple implicit relations relating both the wave amplitude A_w and the wavelength λ_w to the bore intensity. *Chanson* [2009] showed that these relations give a correct estimate of the secondary wave characteristics for undular bore propagating in rectangular channel. For small or moderate Froude numbers, i.e., $1 < Fr < 1.3$, representative of common values observed in estuaries, Lemoine's relations are well approximated by:

$$\frac{\lambda_w}{D_1} = \frac{\sqrt{2}\pi}{\sqrt{3}}(Fr-1)^{-1/2}, \tag{4}$$

$$\frac{A_w}{D_1} = \frac{4}{3\sqrt{3}}(Fr-1), \tag{5}$$

and the wave steepness is given by:

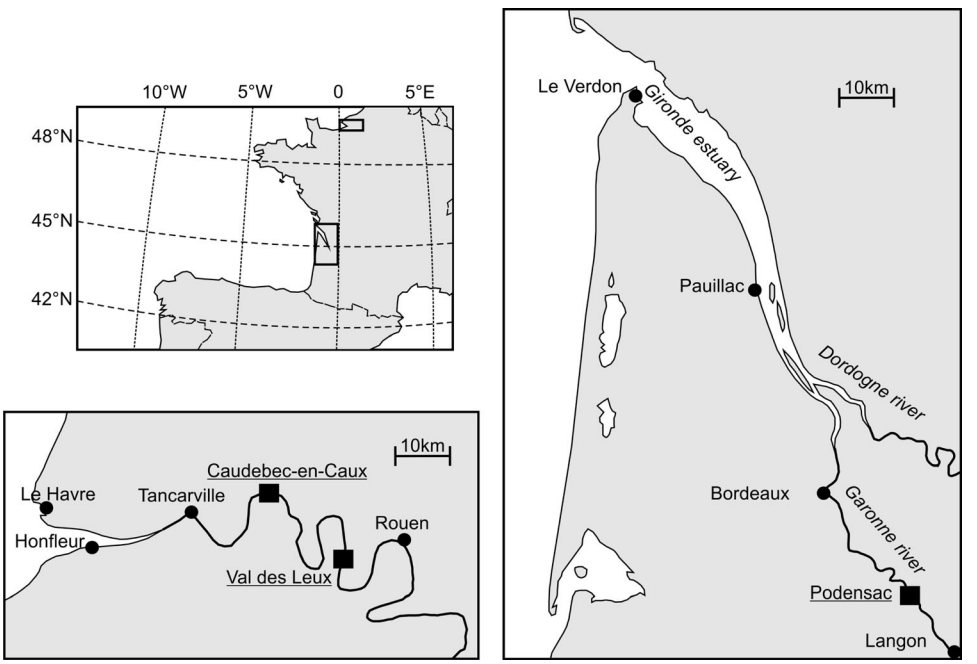

Figure 6. Location map of the Gironde and Seine estuaries. Solid square, field sites.

$$\frac{A_w}{\lambda_w} = \frac{4}{3\sqrt{2\pi}}(Fr-1)^{3/2}. \quad (6)$$

The nondimensional wavelength decreases and the amplitude and steepness increases with increasing Froude number. This is in agreement, at least qualitatively, with the numerous undular bore experiments performed in rectangular channels [e.g., *Favre*, 1935; *Treske*, 1994; *Chanson*, 2009]. These experiments also show that for Froude numbers greater than a critical Froude number, Fr_c, close to 1.25–1.4, the first wave starts to break and the amplitude decreases with increasing Fr. For these undular breaking bores, invisid theories, such Lemoine's, are no longer valid and breaking modeling must be included in nonlinear dispersive bore models [*Tissier et al.*, 2011].

Tidal undular bore behavior in real estuaries will be investigated in section 4.3 and differences with what occurs with undular bores in rectangular channels will be discussed.

3. Field Campaigns and Methods

3.1. Field Sites and Instrument Deployments

Several field experiments have been carried out in 2010 and 2011 in the two main tidal-bore estuaries of the French coast: the Gironde/Garonne and the Seine estuaries (see Figure 6). These campaigns were the first to quantitatively characterize tidal bore formation and propagation in these two estuaries, over a long period of time and for a large range of tidal amplitudes and freshwater discharges. At both sites, tidal bores were of the undular type, always nonbreaking in the Seine River and partially breaking in the Garonne River for the most intense bores.

3.1.1. Gironde/Garonne Estuary

The Gironde estuary is located in the Bay of Biscay, on the southwest coast of France and is formed from the meeting of the Dordogne and Garonne Rivers (see Figure 6). The estuary has a funnel-shaped opening to the Bay of Biscay and a length of about 75 km. During spring tides, the tidal range at the estuary mouth can exceed 5 m. Large amplitude tidal waves propagate in the Garonne and Dordogne rivers up to 160 km from the estuary mouth. Tidal bores, up to 1.5 m high, can form in both the Garonne and the Dordogne Rivers [*Bonneton et al.*, 2012]. Wave breaking, when it occurs, is most of the time limited at the river banks. However, for the most intense tidal bores, several whelps can break with a breaking front, which expands along a large part of the river cross section [*Bonneton et al.*, 2011b]. Atypical undular breaking bores for the Garonne River, with larger Froude numbers, but with much smaller bore jumps (about 0.5 m), can be observed in a narrow and shallow Garonne branch along the Arcins island [*Bonneton et al.*, 2011b; *Chanson et al.*, 2011].

Field experiments were carried out in the Garonne River at Podensac, 126 km upstream the river mouth. This site was selected owing to the presence, during spring tide, of well-developed undular tidal bores and also because the absence of any significant curvature of the river at this location limits the complexity of the tidal bore dynamics. In order to cover a large range of tidal wave amplitudes and freshwater discharges, three campaigns were conducted. The first one, TBG1, was conducted around the spring equinox in 2010 and the two others, TBG2 and TBG3, around the autumn equinoxes in 2010 and 2011. A detailed bathymetric survey of 1 km long was conducted at the field site, in Podensac, at the beginning of each campaign. The cross-sectional river width is 150 m, and the side bank slopes on the right and left banks are, respectively, around 35% and 10%.

3.1.1.1. TBG1

The TBG1 campaign took place during 50 days from 24 February 2010 to 15 April 2010. Flow conditions, in terms of tidal wave elevation and freshwater discharge, are presented in Figure 7. This campaign, starting at the end of winter, was characterized by strong water discharges (Figure 7c), with a mean value of 595 m^3/s and a maximum of 987 m^3/s. As shown in Figure 7b, low tide elevation at the field site $\overline{\zeta}_1$ was weakly dependent on the tidal range at the estuary mouth (Figure 7a) and was mainly controlled by the water discharge (Figure 7c). The mean $\overline{\zeta}_1$ during TBG1 was -0.40 m, corresponding to a cross-sectionally averaged water depth at low tide $D_1 = D(\overline{\zeta}_1) = 4.2$ m.

Instruments were moored along one cross section of the river. Two pressure sensors (Ocean Sensor System), sampled at 10 Hz were deployed in shallow water close to the two river banks. One high-frequency

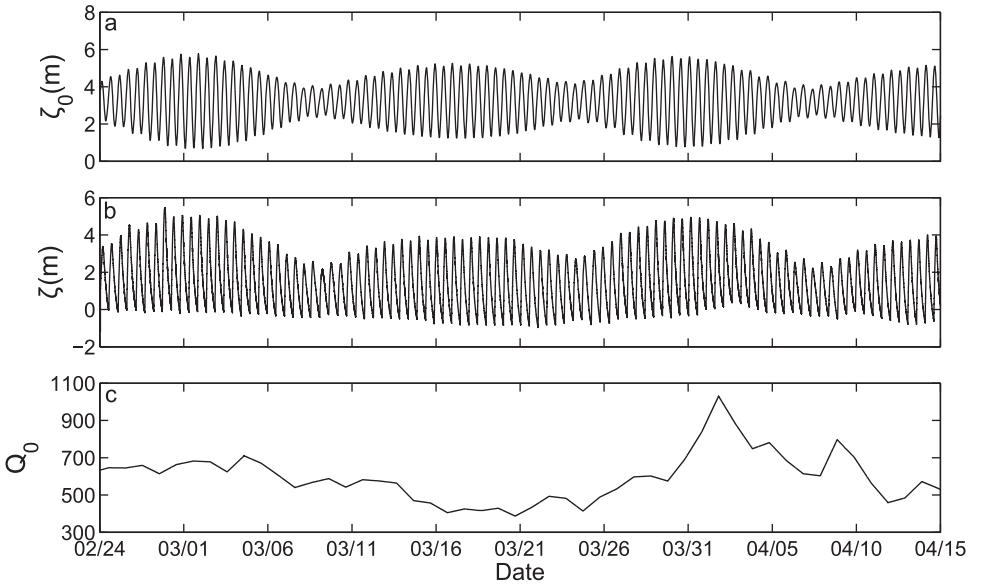

Figure 7. Flow conditions for the TBG1 campaign in the Garonne River, from 24 February 2010 to 15 April 2010. (a) Tidal wave elevation at the estuary mouth; (b) tidal wave elevation at the field site in the upper estuary (Podensac); and (c) freshwater discharge in m^3/s.

1200 kHz bottom-mounted Acoustic Doppler Current Profiler (ADCP-RDI), associated with a near-bottom Acoustic Doppler Velocimeter (ADV Nortek), were deployed in the midchannel and continuously sampled at 2 Hz. The ADCP bin size was set to 0.2 m, and the center of the first bin was located 0.88 m above the river bed. Data were recorded during 17 tides from 24 February 2010 to 5 March 2010, except for one pressure sensor which was deployed until the 15 April (see Figure 7b).

3.1.1.2. TBG2

The TBG2 campaign took place during 52 days from 1 September 2010 to 22 October 2010. This campaign, starting at the end of summer, was characterized by weak water discharges (Figure 8c), with a mean value of 167 m^3/s and a minimum of 79 m^3/s much smaller than annual mean discharge of 610 m^3/s. As previously observed during TBG1, low tide elevation at the field site (Figure 8b) was weakly dependent on the tidal range at the estuary mouth (Figure 8a) and was mainly controlled by the water discharge (Figure 8c). The mean $\bar{\zeta}_1$ value during TBG2 was -1.48 m, a value 1.08 m lower than during TBG1.

During the TBG2 campaign, 17 instruments were set up along three sections of the river spaced at approximately 200 m intervals. The location of the most upstream section corresponded to the location of the TBG1 section. Six pressure sensors were deployed in shallow water and three current profilers (two 1200kHz-ADCP (RDI), one AWAC (Nortek)) were set up along the river axis. The ADCP bin sizes were 0.2 and 0.05 m and the AWAC bin size was 0.5 m. Acoustic velocity measurements were disturbed, generally a few tens of minutes after the bore passage, by high suspended sediment concentrations (larger than 20 g/L). Seven other instruments (three turbidimeters (OBS-3A/Campbell), two Altimeters ALTUS (Ifremer/Micrel), two ADV (Nortek)) were devoted to the analysis of sediment transport processes and river bed evolution (work in progress). Data were recorded during 27 tides from 1 to 14 September 2010, except for one pressure sensor which was deployed until 22 October (see Figure 8b). Pressure sensors were sampled at 10 Hz, ADV at 32 Hz, and the other instruments at 2 Hz. The measurements were supplemented by aerial and boat tidal bore observations between Bordeaux and Podensac on 10 September [*Parisot et al.*, 2012]. Two cameras were also installed on the field site to characterize the phase structure and celerity of the wavefield associated with well-developed undular tidal bores [*Bonneton et al.*, 2011b].

3.1.1.3. TBG3

In order to get complementary tidal bore data for low river discharges, we performed another field experiment in 2011 at the end of summer, from 30 August 2011 to 8 September 2011. The mean water discharge was 135 m^3/s and the mean value of the cross-sectionally averaged water depth at low tide was 2.7 m. Instruments were moored along one cross section of the river. Two current meters were deployed in the midchannel: one high-frequency 1200 kHz bottom-mounted Acoustic Doppler Current Profiler (ADCP-RDI)

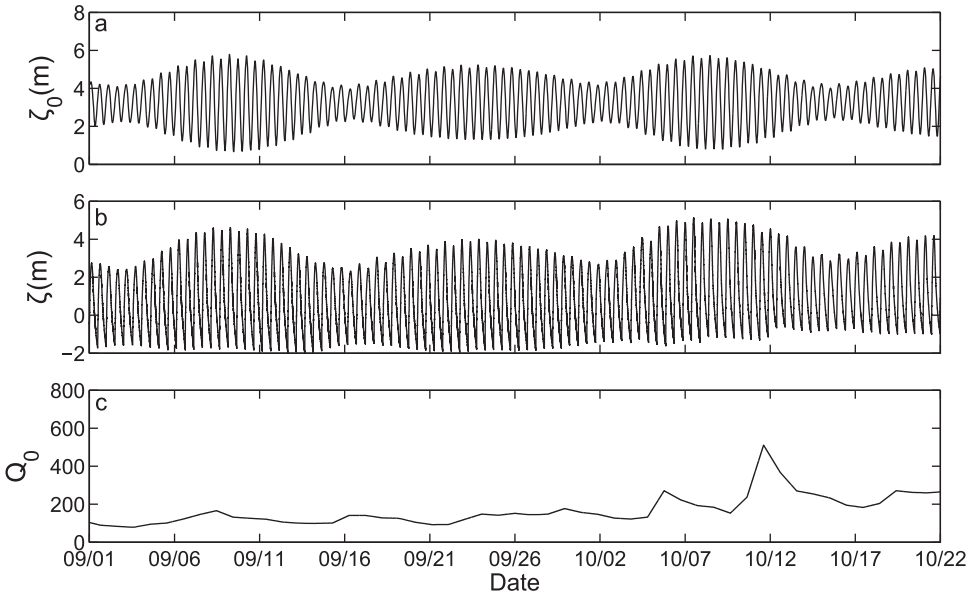

Figure 8. Flow conditions for the TBG2 campaign in the Garonne River, from 1 September 2010 to the 22 October 2010. (a) Tidal wave elevation at the estuary mouth; (b) tidal wave elevation at the field site in the upper estuary (Podensac); and (c) freshwater discharge in m^3/s.

and one ADV (Nortek), sampled at 2 and 32 Hz, respectively. The ADCP bin size was set to 0.1 m and the center of the first bin was located 0.79 m above the river bed. Three pressure sensors, sampled at 10 Hz were deployed along the river cross section in shallow water close to the two river banks and one in the midchannel.

3.1.2. Seine Estuary

The Seine estuary is located in the northwestern part of France (see Figure 6). The downstream part of the Seine estuary is funnel shaped with a mouth that opens toward the west of Baie de Seine. Tidal range at the estuary mouth can reach 8.5 m during spring tides and the tides influence the estuary up to 160 km from the mouth. An intense tidal bore was frequently observed in the past, but due to river training and dredging during the last two centuries, its amplitude has dramatically decreased [*Bonneton et al*., 2012].

In order to quantitatively analyze tidal bore occurrence in the Seine River, we carried out pressure measurements (10 Hz sampling rate) from 25 August 2011 to 13 September 2011. We chose two field sites in the Seine River. The first was located in Caudebec-en-Caux (55 km upstream from the estuary mouth), which was the location where tidal bore intensity reached its maximum amplitude until the mid-1960s. The second one was located in Val des Leux, 100 km upstream from the estuary. We did not observe tidal bore at Caudebec-en Caux even for the highest spring tide. However, further upstream at Val des Leux significant tidal bores were identified [*Bonneton et al*., 2012]. At this location, the cross-sectional width is 270 m, and the side bank slopes on the right and left banks are, respectively, around 14% and 23%. During the campaign, the mean water discharge of 216 m^3/s was significantly smaller than the annual mean discharge of 365 m^3/s. The mean value of the cross-sectionally averaged water depth at low tide was 7.7 m, a value much larger than those of the Garonne field site.

3.2. Methods

3.2.1. Water Elevation Measurements

An absolute centimetric DGPS positioning of the water surface elevation was performed at low tide for the four campaigns. Continuous water elevation measurements were carried out with two different methods. The first one was based on direct acoustic surface tracking measurements (AWAC, Nortek). With this method, we recorded surface elevation for 14 large amplitude tides, from 7 to 13 September 2010 (TBG2 campaign). However, most of the water depth and surface elevation data presented in this paper were obtained from 10 Hz-pressure sensor measurements. For tidal waves without bore, the water depth can be accurately estimated assuming that the pressure field is hydrostatic. However, in the presence of tidal bores, this hypothesis is no longer valid. Indeed, as explained in sections 2.2 and 2.3, this phenomenon is basically

nonhydrostatic. The intensity of nonhydrostatic effects can be characterized by the shallowness parameter: $\mu=2\pi D_1/\lambda_w$, which, using the equation (4), can be expressed as a function of the Froude number: $\mu=\sqrt{6}(Fr-1)^{1/2}$. For large Froude numbers, close to the critical Froude number, Fr_c, wavefield nonhydrostaticity is significant. To take into account this effect, we use a classical approach based on linear wave theory. The pressure time signal associated with the tidal bore secondary wavefield is transformed to the frequency domain by a Fourier decomposition. The elevation of each wave component $\hat{\zeta}(f)$, for frequency f between 0.05 and 0.5 Hz, is evaluated taking into account a nonhydrostatic correction: $\hat{\zeta}(f)=\frac{\cosh(kD)}{\cosh(kZ_c)}\hat{\zeta}_{hydro}$, where k is the wave number and Z_c the height of the pressure sensor from the bed. The corrected water depth signal is then computed from an inverse Fourier transform. In order to validate this approach, we have compared these water depth estimates with direct acoustic surface tracking measurements obtained during TBG2. For the largest observed Froude numbers, corresponding to the highest nonlinearity and nonhydrostaticity effects, the maximum error for wave amplitude estimation is less than 10%.

3.2.2. Tidal Bore Characterization

3.2.2.1. Tidal Bore Occurrence

As shown in section 2.2, it is difficult to accurately determine the onset of tidal bore formation, because it is a gradual physical process. However, the transition between a tidal wave regime without bore (e.g., Figure 4a) and a well-developed undular tidal bore regime (e.g., Figure 4h) is associated with an increase of the maximum elevation slope up to 1 order of magnitude. Based on our multisite database, we consider hereafter that a tidal bore is well formed when the maximum elevation slope, α_m, is larger than 10^{-3}. Below this threshold, very low intensity tidal bores will not be considered. For instance, the embryonic tidal bores presented in Figures 4f and 4g are not selected. We will see in section 4.3 that this threshold slope condition corresponds to select tidal bores such as $Fr>1.03$.

3.2.2.2. Froude Number

As presented in section 2.3, the intensity of the primary wave (i.e., mean jump) is characterized by the Froude number $Fr=\frac{|u_1-c_b|}{(gD1)^{1/2}}$, where c_b is the bore celerity and u_1 and D_1 are the cross-sectionally averaged velocity and water depth ahead of the bore. All these bore variables were synchronously measured during the TBG2 campaign, from 1 to 14 September 2010. For the other Garonne and Seine observations, the Froude numbers were evaluated from elevation measurements and considering conservation of mass and momentum across the mean jump. The Froude number is then given by the expression:

$$Fr^2=\frac{A_2}{A_1D_1}\left(\frac{K_2-K_1}{A_2-A_1}\right), \tag{7}$$

where, $A(\bar{\zeta})$ is the cross-sectional area and $K(\bar{\zeta})=\int_{\zeta_b}^{\bar{\zeta}}A\mathrm{d}\zeta$ (see Figure 5 for the variable definitions).

The accuracy of this Froude number evaluation was assessed in comparison with direct measurements of the Froude number obtained during the TBG2 campaign. The bore celerity was evaluated from the phase lag between two 10 Hz-synchronized pressure sensors deployed along the Garonne River. The two sensors were separated by a distance of 200 m. An estimate of cross-sectionally averaged velocities were obtained using the depth-averaged velocities measured with the current meter profilers. We found that the agreement between direct measurements of the Froude number and its evaluation from relation (7) is good with a maximum error of 5%.

4. Results

This section is organized in the same way as the *Physical background* section 2, where tidal bore processes are presented from large scale (i.e., estuarine scale) to small scale (i.e., secondary wave scale).

4.1. Freshwater Discharge Effects

In section 2.1, we have analyzed tidal wave transformation and its consequence in terms of tidal bore occurrence in a simplified context for which freshwater discharge effects are neglected. However, it is well known that tide in estuaries may be significantly affected by the rate of discharge [e.g., *Horrevoets et al*., 2004]. This phenomenon can be clearly illustrated by comparing the tidal wave evolution in the Gironde/Garonne estuary during both the TBG1 and TBG2 campaigns, which are characterized by very different discharges, Q_0. Thus, we present in Figure 9 the tide evolution over one tidal cycle, for contrasting freshwater discharges

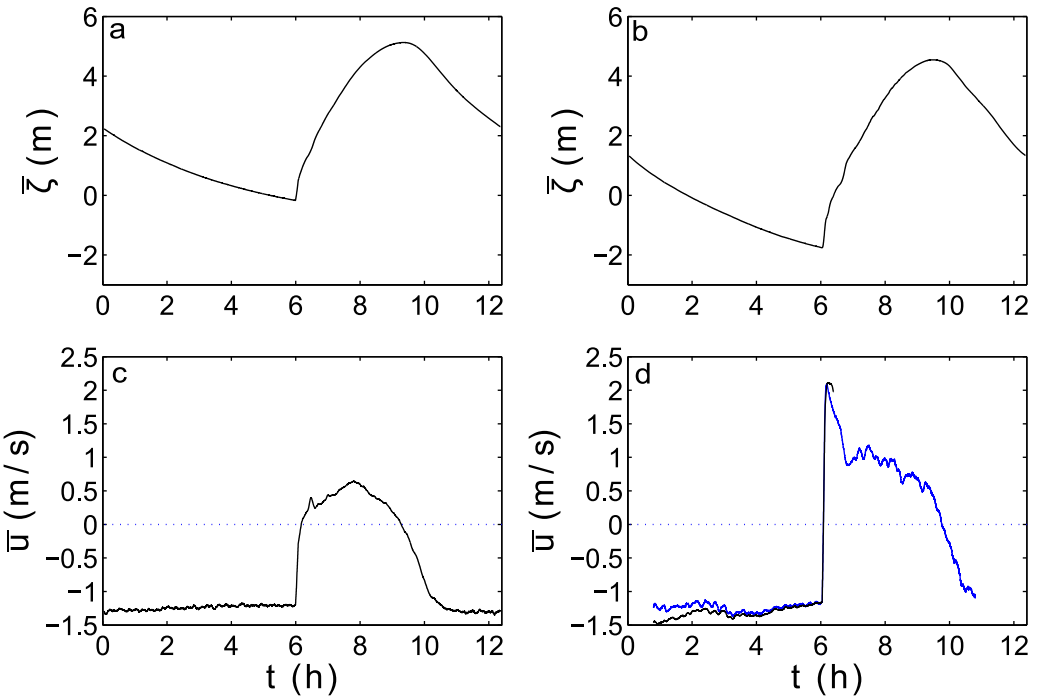

Figure 9. Tidal wave evolution at the Garonne field site (Podensac) over one tidal cycle, for large spring tidal ranges at the estuary mouth and contrasting river discharges. (a and c) TBG1 campaign, 2 March 2010, $Tr_0 = 5.06$ m, $Q_0 = 681$ m^3/s; (b and d) TBG2 campaign, 10 September 2010, $Tr_0 = 5.02$ m, $Q_0 = 128$ m^3/s (a and b). The 5 min time-averaged elevation $\bar{\zeta}$. (c) 5 min time-averaged depth-integrated along-channel velocity. (d) black line, 5 min time-averaged depth-integrated along-channel velocity; blue line, 5 min time-averaged along-channel velocity in one bin located at 1.5 m above the river bed.

and the same spring tidal range at the estuary mouth. In both cases, a tidal bore was formed. For small Q_0 (TBG2), the tidal range increases significantly from 5.02 m at the estuary mouth to 6.33 m at the upper estuary field site (Figure 9b), while for large Q_0 (TBG1), the tidal range was virtually constant with a very small increased from 5.06 m at the estuary mouth to 5.16 m at the field site (Figure 9a). The tidal wave asymmetry, for both the elevation and the current, was also much stronger for low Q_0 than for high Q_0. Whatever the river discharge, the 5 min time-averaged depth-integrated along-channel velocity, $\bar{u}$, was nearly constant during ebb tide around a value of -1.2 m/s. This downstream current, practically independent on the river discharge, must be considered as a component of the global tidal wavefield. Thus, it differs significantly from adverse currents, u_1, imposed in classical laboratory bore experiments. At the beginning of the flood, we observe a much faster growth of the velocity for TBG2 than TBG1 (see Figures 9c and 9d). During TBG1, the velocity evolved in 110 min from -1.20 m/s just before the bore passage to a maximum flood velocity of 0.64 m/s. During TBG2, the velocity evolved in 9 min from -1.13 m/s just before the bore passage to a maximum flood velocity of 2.07 m/s.

Figure 10a shows the evolution, for TBG1 and TBG2 campaigns, of the tidal amplification ratio, $(Tr-Tr_0)/Tr_0$, as a function of the tidal range at the estuary mouth Tr_0. For the two campaigns, we observe an amplification of the tidal wave in the upper estuary (i.e., $(Tr-Tr_0)/Tr_0 > 0$), which results from the dominance of estuary convergence over friction effects. The tidal amplification ratio is a decreasing function of the tidal range at the estuary mouth. For neap tide, $(Tr-Tr_0)/Tr_0$ can reach values of up to 130%. The influence of freshwater discharge on this tidal wave amplification process is clearly illustrated in Figure 10a. There is a continuous decrease of the ratio $(Tr-Tr_0)/Tr_0$ with increasing Q_0. The tidal wave amplification mechanism, related to estuary convergence, is offset by tidal wave damping due to significant freshwater discharges. Small discharges are then favorable to tidal wave amplification in the estuary, and as a result favorable to tidal bore formation. For instance, we can see in Figure 10b that for the same Tr_0, a tidal bore can form during the low-discharge TBG2 campaign and not during the high-discharge TBG1 campaign. During TBG2, tidal bores can even form at neap tide for very small Tr_0, up to 1.9 m. Figure 10b shows that the tidal bore occurrence is much more dependent on the local tidal range than on Tr_0. The transition between no-bore and bore regimes takes place for Tr around 3.8–4.8 m, whatever the freshwater discharge conditions.

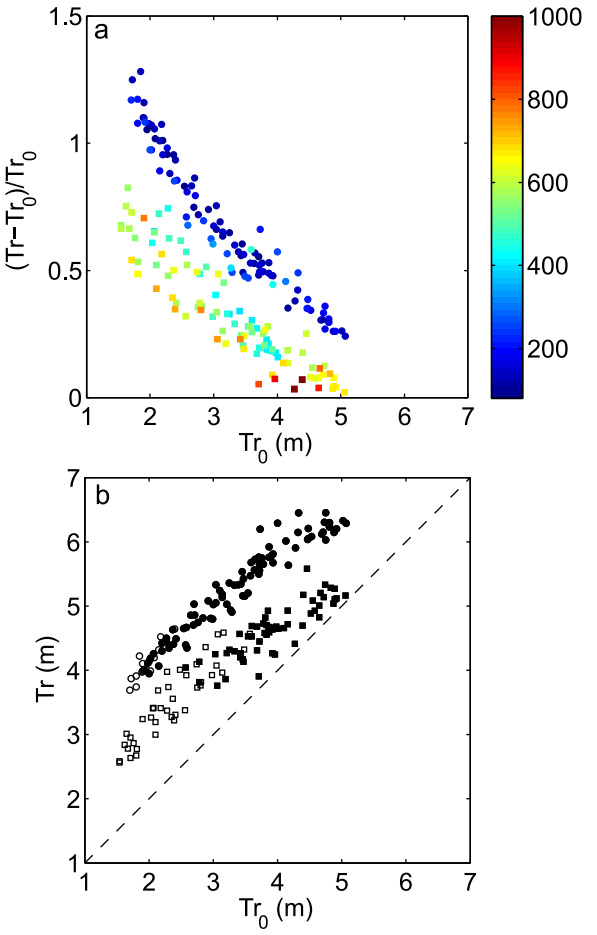

Figure 10. (a) tidal amplification ratio $(Tr-Tr_0)/Tr_0$ as a function of Tr_0; the colormap shows the freshwater discharge, Q_0, in m^3/s. (b) tidal range at the Garonne field site, Tr, as a function of Tr_0; close and open symbols correspond to tidal wave regimes with and without tidal bore respectively. Square symbol, TBG1 campaign; circle symbol, TBG2 campaign.

Contrary to what is often assumed [*Chanson*, 2012], tidal bores can also occur for high water discharges, for instance, up to $Q_0 = 987 m^3/s$ in the Garonne River (5.6 times the mean discharge in August, the driest month).

An important variable controlling the tidal bore intensity locally is the water depth just before bore arrival $D_1 = D(\bar{\zeta}_1)$ (i.e., low tide water depth). We can see in Figures 7b and 8b that the low tide elevation, $\bar{\zeta}_1$, which is weakly dependent on Tr_0, is strongly controlled by the water discharge. The mean value of $\bar{\zeta}_1$ over a campaign decreased by 1.08 m from TBG1 to TBG2, as the mean water discharge decreased from 595 to 167 m^3/s.

4.2. Tidal Bore Intensity as a Function of the Local Dimensionless Tidal Range

In the upper estuary, at a local scale, the two main flow variables controlling nonlinear tidal wave transformation and bore formation are Tr and D_1. We can reasonably expect that the mean tidal bore in the upper estuary is mainly governed by the dimensionless local parameter $\epsilon = Tr/D_1$, which can be considered as a local measure of tidal wave nonlinearity.

To further test this hypothesis, we analyze the mean bore intensity as a function of this dimensionless parameter for the three campaigns carried out in the Garonne River, which corresponded to different freshwater discharge conditions. Figure 11 presents the evolution of the maximum elevation slope at the tidal bore wave front, α_m, as a function of ϵ. This slope is evaluated from the relation $\alpha_m = \frac{1}{c_b}\delta_m$, where c_b is the bore celerity and δ_m is defined in Figure 5. Figure 11 shows a clear relationship between α_m and ϵ. A given dimensionless tidal range corresponds to a given bore slope, whatever the freshwater discharge. The bore slope is an increasing function of the nonlinear parameter ϵ. A similar relationship is observed in Figure 12 between the tidal bore Froude number and ϵ. Figures 11 and 12 suggest that the tidal bore intensity is mainly governed by the local nonlinear parameter ϵ. We do not observe in these figures any significant variation of tidal bore intensity as a function of the freshwater discharge. This does not mean that tidal bore intensity is independent on Q_0, but that this dependence is mainly related to the relationship between ϵ and Q_0 (see section 4.1).

4.3. Secondary Wavefield

We present in Figure 13 the evolution of the maximum elevation slope at the tidal bore wave front, α_m, as a function of the Froude number of the mean tidal bore. This figure shows a clear relationship between the two variables, regardless of the freshwater discharge conditions and the field site (Garonne or Seine rivers). The tidal bore slope α_m follows approximately a $(Fr-1)^{3/2}$ power law, in accordance with the theoretical law for secondary wave steepness given by equation (6). However, a transition can be observed around a Froude number, F_T, of about 1.1, with an abrupt decrease of α_m by a factor of about 2 when Fr goes below F_T.

We then analyze the characteristic scales of the first wave train. As described in *Bonneton et al.* [2011a, 2011b], there is a strong variability of the secondary wavefield along the river cross section. In the present

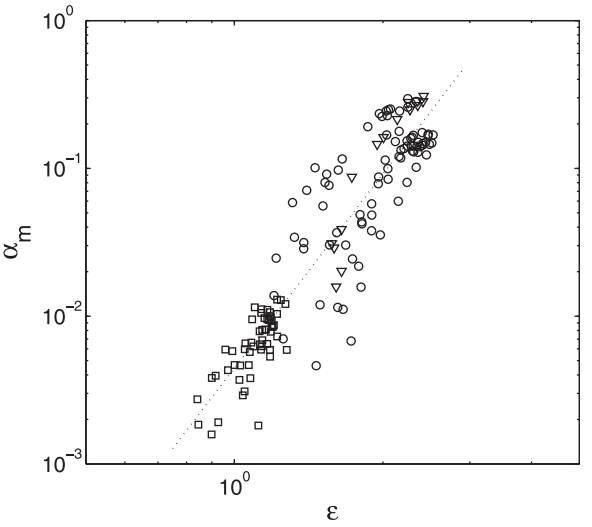

Figure 11. Maximum elevation slope at the tidal bore wave front, α_m, as a function of the nondimensional tidal range, $\epsilon = Tr/D_1$. Square, TBG1 campaign; circle, TBG2 campaign; triangle, TBG3 campaign. Dotted line, linear fit.

paper, we focus our analysis on the wave structure in the midchannel. The wave period, T_w, and the amplitude, A_w, are defined in Figure 5. The wavelength, λ_w, is estimated by using the relation: $\lambda_w = c_b T_w$. The data acquired during the four campaigns are compared with laboratory data for undular bores propagating in rectangular channels [*Favre*, 1935; *Treske*, 1994]. We select the field data corresponding to measurements in the axis of the river, except for those from the Seine River. The evolution of the nondimensional wavelength, λ_w/D_1, as a function of the Froude number, is presented in Figure 14. Once again we can identify a transition around $F_T = 1.1$. On the one hand, for large Froude numbers, $Fr > F_T$, we can observe a good agreement between field measurements, laboratory data, the Lemoine theory and the approximate equation (4). On the other hand, for $Fr < F_T$, the wavelengths measured in the field are much larger than those from laboratory data and Lemoine's predictions. Just below F_T, λ_w/D_1 increases abruptly by a factor of about 2. The evolution of the secondary wave steepness as a function of Fr is presented in Figure 15 which shows the same trend as for Figure 13. For $Fr > F_T$, the wave steepness measured in the field is in agreement with laboratory data and the approximate equation (6). The secondary wavefield transition around F_T is in accordance with that observed by *Treske* [1994] for undular bore propagating in a trapezoidal channel with an embankment slope $\beta = 1/3$ and a bottom width, W, of 1.24 m. The bank slope and W/D_1 values in *Treske* [1994] are close to those in our field sites. With these laboratory conditions *Treske* [1994] found a transition Froude number, $F_T = 1.15$, very close to what we observed in the field. These results show that tidal bore whelps, in the midchannel, differ significantly from those in rectangular channels [*Favre*, 1935; *Treske*, 1994; *Chanson*, 2009]. This observation can be explained by the strong interaction between the secondary wavefield and the low sloping estuarine banks. The value observed for the transition Froude number F_T, in our field experiments and in Treske's laboratory study, can not prevail for all estuarine environments and certainly depends on the characteristic geometric scales of the river cross section: β and W/D_1.

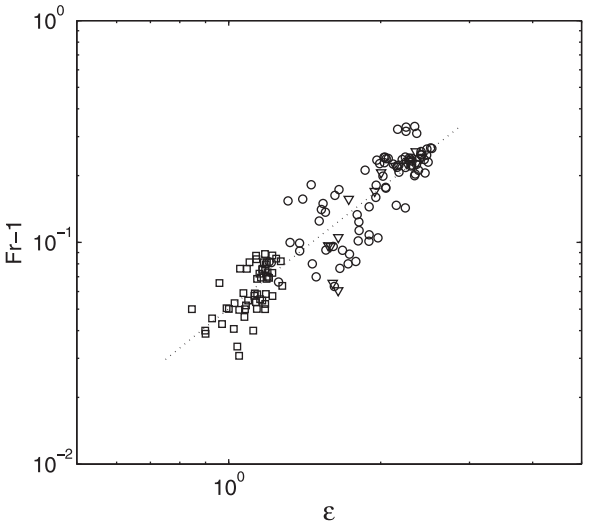

Figure 12. Evolution of the Froude number minus 1, as a function of the nondimensional tidal range, $\epsilon = Tr/D_1$. Square, TBG1 campaign; circle, TBG2 campaign; triangle, TBG3 campaign. Dotted line, linear fit.

After this analysis of the first wave train characteristics as a function of Fr, the two last figures present elevation and velocity time signals of the secondary wavefield over several wave periods. These figures correspond to two tidal bores formed from the same high spring tidal range, $Tr_0 \simeq 5$m, but from contrasting freshwater discharges.

For low Q_0, we observe in Figure 16 a well-developed undular tidal bore with a Froude number of 1.24. At the wave front passage, the along-

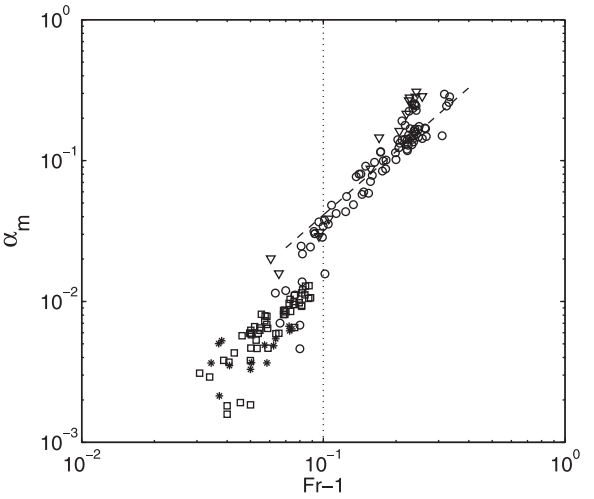

Figure 13. Maximum elevation slope at the tidal bore wave front, α_m, as a function of the Froude number minus 1. Square, TBG1 campaign; circle, TBG2 campaign; triangle, TBG3 campaign; asterisk, Seine campaign. Dashed line, $(Fr-1)^{3/2}$ power law; dotted line, transition around $Fr \simeq 1.1$.

channel velocity increases abruptly from −1 to 1.4 m/s in 2.5 s. This corresponds to a maximum acceleration at the wave front of 1.75 m s^{-2}. The whelps are associated with significant vertical motion with vertical velocity ranging from −0.25 to 0.25 m/s. We can see in Figure 16 that the along-channel velocity and the elevation signals are in phase as previously observed by *Furgerot et al.* [2013]. The secondary wavefield, of period 2.5–3 s, is characterized by well-defined wave groups with a period of about 40 s. The same secondary wavefield modulation can be observed for the two neighboring tides, whose tidal ranges Tr_0 are close to 5 m.

Figure 17 present the tidal bore wavefield for the same tidal range, $Tr_0 \simeq 5$.m, but for large freshwater discharge. We observe in this figure a low-intensity undular tidal bore with a Froude number of 1.08. At the wave front passage, the along-channel velocity increases from −1.2 to −0.5 m/s in 12 s. It is important to note that for such large Q_0 the velocity remains negative (seaward directed) after the bore passage (Figure 17b). The velocity becomes positive during the rising tide 10 min after the bore (see Figure 9). Once again we can note in Figure 17 that the along-channel velocity and the elevation signals are in phase.

5. Conclusion and Perspectives

We presented in this paper an analysis on tidal bore formation and propagation in funnel-shaped estuaries as a whole, from large-scale tidal wave transformation to small-scale wave processes associated with tidal bores.

Tidal bore formation results from the large-scale nonlinear distortion of a tidal wave propagating upstream a convergent estuary. From a scaling analysis of the nonlinear shallow water equations, we showed that tidal bore formation is mainly governed by the dimensionless dissipative parameter $\mathcal{D}_i$, which characterizes the intensity of tidal wave nonlinearity. Table 2 presents the geometric and tidal properties of six regularly funnel-shaped estuaries (i.e., estuaries characterized by only one convergence length scale) where tidal bores have been documented: the Gironde/Garonne, the Hooghly, the Humber, the Pungue, the Qiantang, and the Severn estuaries. This table confirms that tidal-bore estuaries are characterized by large values of $\mathcal{D}_i$ compared with observations for a large number of convergent estuaries over the world [*Lanzoni and Seminara*, 1998; *Toffolon et al.*, 2006]. Tidal-bore estuaries listed in Table 2 are characterized by significant channel convergence, with $K \simeq 1$. We showed that for such convergence, the dissipative parameter $\mathcal{D}_i$ can be expressed in a simple way in terms of the characteristic external scales of the problem:

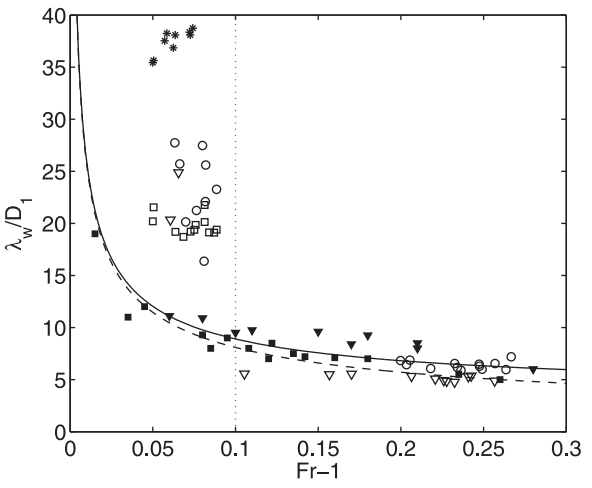

Figure 14. Nondimensional wavelength as a function of the Froude number minus 1. Square, TBG1 campaign; circle, TBG2 campaign; triangle, TBG3 campaign; asterisk, Seine campaign; solid square, *Treske* [1994] experiment; solid triangle, *Favre* [1935] experiment. Continuous line, *Lemoine* [1948] theory; dashed line, approximate equation (4); dotted lines, transition around $Fr \simeq 1.1$.

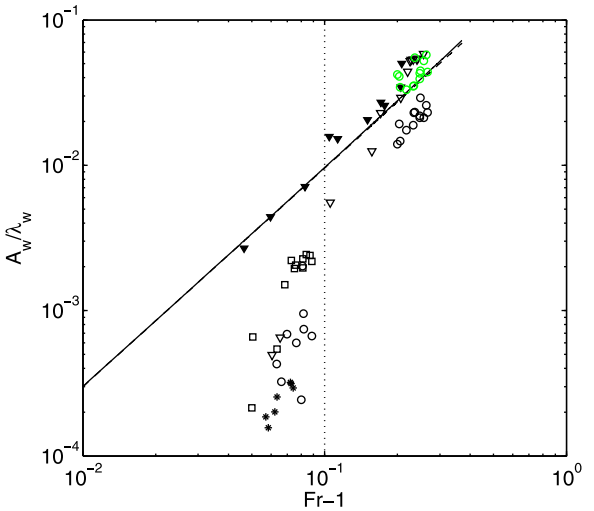

Figure 15. Wave steepness as a function of the Froude number minus 1. Square, TBG1 campaign; open circle, TBG2 campaign (green open circle, wave steepness based on the maximum amplitude, i.e., 5 or 6th wave); triangle, TBG3 campaign; asterisk, Seine campaign; solid square, *Treske* [1994] experiment; solid triangle, *Favre* [1935] experiment. Continuous line, *Lemoine* [1948] theory; dashed line, approximate equation (4); dotted lines, transition around $Fr \simeq 1.1$.

$$\mathcal{D}_i^* = C_{f0}\frac{A_0 L_{b0}}{D_0^2}.$$

Table 2 shows that this expression gives a good estimate of $\mathcal{D}_i$ for tidal-bore estuaries, except for the Pungue estuary which is characterized by a moderate convergence (i.e., K significantly smaller than 1). The $\mathcal{D}_i^*$ parameter, which characterizes the intensity of tidal wave nonlinearity, is enhanced for increasing tidal range, friction coefficient and convergence length and decreasing water depth. When this parameter is large, i.e., $\mathcal{D}_i^* > 1.7$ (see Table 2), the funnel-shaped estuaries are strongly dissipative and the conditions are favorable to tidal bore formation. The strong dependence of $\mathcal{D}_i^*$ on the water depth explains why estuary dredging can significantly reduce tidal wave nonlinearity and then tidal bore occurrence, as observed in the Seine River [*Bonneton et al.*, 2012] and the Colorado River [*Bartsch-Winkler and Lynch*, 1988]. The present scaling analysis is useful to classify the global tidal wave dynamics in funnel-shaped estuaries and gives qualitative information about bore occurrence. However, it would be oversimplified to quantitatively evaluate it. First of all, the convergence L_b and the mean water depth D can evolve along the estuary. For instance, if the width of the Pungue estuary is well described by a simple exponential law [*Graas and Savenije*, 2008], some tidal-bore estuaries, such as the Dee estuary [*Simpson et al.*, 2004], the Mont Saint Michel estuary [*Furgerot et al.*, 2013], and the Seine estuary can not be described by only one convergence length scale. For instance, the Seine estuary is characterized by two different convergence lengths: a small one for the lower estuary ($L_b = 7$ km) and a larger one for the middle/upper estuary ($L_b = 110$ km). In accordance with equation (3), the lower estuary is weakly dissipative and the middle/upper estuary is strongly dissipative and then favorable to tidal bore formation. However, the most restrictive assumption is to consider a constant water depth D_0. Indeed, tidal bores are dependent on local bathymetry variations, with an increase of bore intensity with decreasing water depth. Nevertheless, the scaling analysis presented in this paper is a valuable first step toward the characterization of large-scale tidal bore formation in terms of the relevant global dimensionless parameters characterizing estuarine hydrodynamics.

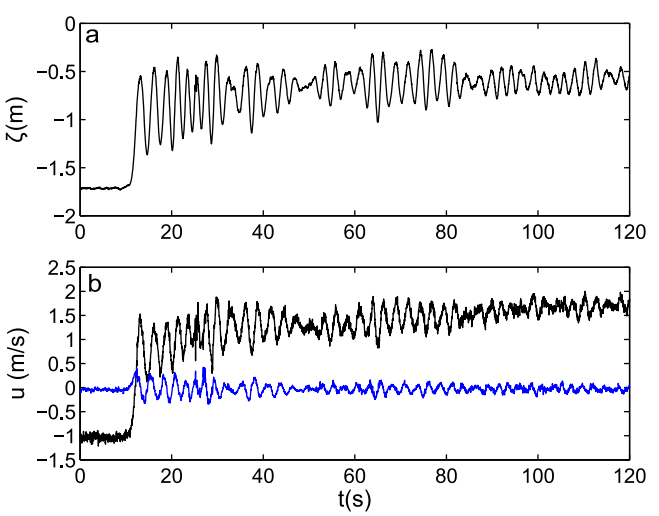

Figure 16. Tidal bore at the Garonne field site (Podensac) for a large spring tidal range at the estuary mouth ($Tr_0 = 5.0$ m), and low river discharge ($Q_0 = 106\,m^3/s$). TBG3 campaign, 31 August 2011. Measurements from an ADV current meter sampled at 32 Hz. (a) Surface elevation ζ; (b) velocity components measured at 1.2 m above the river bed (along-channel component in black and vertical component in blue).

After this global tidal wave scaling analysis, we carried out a quantitative investigation of tidal bore dynamics in the two main French tidal-bore estuaries: the Seine and Gironde/Garonne estuaries. For the first time, long-term tidal bore experiments were carried out during several neap-spring tide cycles and for contrasting water

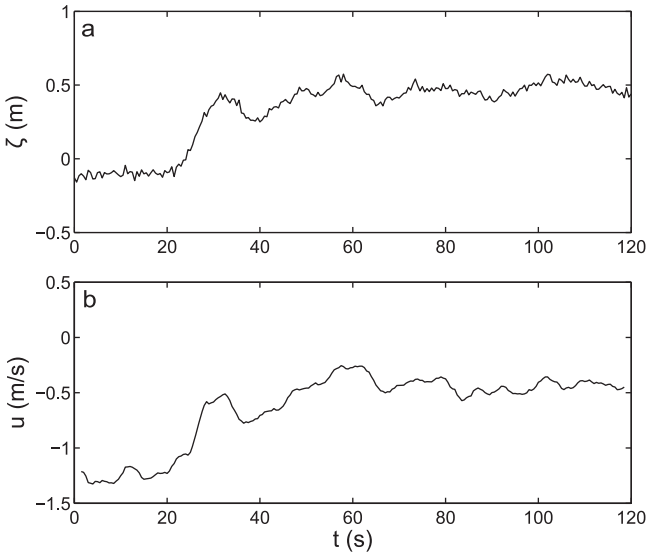

Figure 17. Tidal bore at the Garonne field site (Podensac), for a large spring tidal range at the estuary mouth ($Tr_0 = 5.1$ m), and large river discharge ($Q_0 = 681$ m^3/s). Measurements from an ADCP current meter sampled at 2 Hz. TBG1 campaign, 2 March 2010. (a) Surface elevation ζ; (b) depth-integrated along-channel velocity u.

discharges (observations for more than 200 tides). We described the effect of freshwater discharge, Q_0, on tidal wave amplification and on tidal bore occurrence. The freshwater discharge damps the tidal wave and thus limits tidal bore development in the upper estuary. We showed that tidal bore intensity is mainly governed by the dimensionless tidal range $\epsilon = Tr/D_1$, which characterizes the local tidal wave nonlinearity. The ϵ parameter is a decreasing function of freshwater discharge, as Tr and D_1 are, respectively, decreasing and increasing functions of Q_0.

We also analyzed the evolution of secondary wave characteristic scales as a function of the Froude number of the primary wave (i.e., mean jump). We observed classical undular bore trends: the dimensionless wavelength and the wave steepness respectively decrease and increase with increasing Fr. However, we identified two different regimes around a transition Froude number, F_T, of about 1.1. On the one hand, for $Fr > F_T$, the whelp characteristics in the midchannel are similar to those observed for undular bores generated in rectangular channels and are in agreement with *Lemoine*'s [1948] theory. On the other hand, for $Fr < F_T$, the dimensionless wavelength λ_w/D_1 is much larger and the wave steepness A_w/λ_w much smaller than what is commonly observed in rectangular channels with a similar Froude number. The transition around F_T occurs quite abruptly and λ_w/D_1 increases by a factor of about 2 when Fr goes bellow F_T. This whelp field transition is in accordance with that observed by *Treske* [1994] for undular bores propagating in a trapezoidal channel. He found a transition Froude number, $F_T = 1.15$, very close to what we observed in the field. These results show that tidal bore whelps, in the midchannel, differ significantly from those in rectangular channels. This is because tidal bores strongly interact with the gently sloping river banks.

This transition can partly explain why tidal bore occurrence in estuaries is most likely underestimated. Indeed, most of tidal bore observations worldwide are based on visual observations [*Lynch*, 1982; *Bartsch-Winkler and Lynch*, 1988; *Chanson*, 2012], which are very sensitive to whelp steepness. The abrupt steepness decrease when Fr goes below F_T makes it difficult to visually observe tidal bores. Our quantitative long-term measurements allowed us to show that tidal bores occur in the Garonne River for a large majority of tides, and can even form during neap tides (for low Q_0) or during high freshwater discharge conditions (for high Tr_0). Tidal bores are also still present in the Seine River even if their wave steepness is too small to be visually observed. It is important to identify and to characterize such tidal bores because, even if their whelps are of low intensity, they can be associated to a significant mean jump (see Figure 17) and then play a significant role in the upper estuary dynamics.

Our findings in the Gironde/Garonne and the Seine estuaries should encourage new quantitative field observations to reassess tidal bore occurrence in estuaries worldwide. In parallel with these new observations, it would be important to develop a scaling analysis for bore formation which goes beyond the one presented in section 2.1 by taking into account freshwater discharge and spatial variations of the estuary water depth. Such analysis could also benefit from the recent advances in nonlinear dispersive wave modeling [*Bonneton et al*., 2011c], which now provide us efficient tools to simulate tidal bore in real estuaries.

Appendix A: Nondimensionalized Tidal Wave Equations

The cross-sectionally integrated equations (Saint Venant equations) for tidal waves propagating in a channel characterized by a horizontal bottom and an exponentially decreasing width (see Figure 1) may be expressed as:

$$\frac{\partial \zeta}{\partial t}+u\frac{\partial \zeta}{\partial x}+D\frac{\partial u}{\partial x}-\frac{uD}{L_{b0}}=0, \tag{A1}$$

$$\frac{\partial u}{\partial t}+u\frac{\partial u}{\partial x}+g\frac{\partial \zeta}{\partial x}+C_{f0}\frac{|u|u}{D}=0, \tag{A2}$$

where ζ is the surface elevation, D the cross-sectionally averaged water depth, u the cross-sectionally averaged velocity, L_{b0} the convergence length, C_{f0} the friction coefficient, and g the gravity.

Tidal flows in convergent estuaries are controlled by the external variables: D_0, T_0, A_0, L_{b0}, and C_{f0}, which are known a priori for any particular estuary. The velocity scale, U_0, and the length scale, L_0, cannot be prescribed a priori since they depend on the channel response to a given forcing. These two variables are functions of the external variables.

We introduce the following scaling:

$$x=L_0x',\ \ t=\omega_0^{-1}t',\ \ D=D_0D',\ \ \zeta=A_0\zeta',\ \ u=U_0u'.$$

The equations of motion then become (after dropping the primes for the sake of clarity):

$$\frac{\partial \zeta}{\partial t}+\frac{K}{\mathcal{L}}\left(\epsilon_0 u\frac{\partial \zeta}{\partial x}+D\frac{\partial u}{\partial x}\right)-KuD=0, \tag{A3}$$

$$\frac{\partial u}{\partial t}+\frac{K}{\mathcal{L}}\epsilon_0 u\frac{\partial u}{\partial x}+\frac{1}{K\mathcal{L}}\delta_0^2\frac{\partial \zeta}{\partial x}+\underbrace{K\gamma_0}_{\mathcal{D}_i}\frac{|u|u}{D}=0. \tag{A4}$$

These nondimensional equations are controlled by three independent external dimensionless parameters: $\epsilon_0=\frac{A_0}{D_0}$, $\delta_0=\frac{(gD_0)^{1/2}\omega_0^{-1}}{L_{b0}}$ and $\gamma_0=\frac{C_{f0}A_0L_{b0}}{D_0^2}$. The convergence parameter $K=\frac{U_0}{L_{b0}A_0D_0^{-1}\omega_0}$ and the dimensionless parameter $\mathcal{L}=\frac{L_0}{L_{b0}}$ are unknown functions of the three external dimensionless parameters: ϵ_0, δ_0, γ_0. For tidal-bore estuaries, the hypothesis $K=1$ (i.e., balance between temporal variation of ζ and channel convergence) is well supported by field observations (see Table 2). In this case, the velocity scale is given by:

$$U_0=\frac{L_{b0}A_0\omega_0}{D_0},$$

and the dissipative parameter $\mathcal{D}_i$ can be expressed in function of the external variables as follow:

$$\mathcal{D}_i=\gamma_0=C_{f0}\frac{A_0L_{b0}}{D_0^2}$$

Acknowledgments

This work was undertaken within the framework of the Project MASCARET (Région Aquitaine), with additional financial support from Bordeaux University. The authors are thankful to all the people involved in this experiment. In particular, we would like to thank G. Detandt, G. Oggian, N. Pochon, A. Sottolichio, and J. Van de Loock. The authors acknowledge VNF Cadillac for their technical support for the mooring and Y. Lavigne for the aerial photographs. The data presented in this paper can be obtained by contacting Philippe Bonneton (p.bonneton@epoc.u-bordeaux1.fr).

References

Bartsch-Winkler, S., and D. K. Lynch (1988), *Catalog of Worldwide Tidal Bore Occurrences and Characteristics*, U.S. Gov. Print. Off. [Available at http://pubs.er.usgs.gov/publication/cir1022.]

Benjamin, T. B., and M. J. Lighthill (1954), On cnoidal waves and bores, *Proc. R. Soc. London, Ser. A*, *224*(1159), 448–460.

Bonneton, N., P. Bonneton, J.-P. Parisot, A. Sottolichio, and G. Detandt(2012), Tidal bore and Mascaret—Example of Garonne and Seine Rivers, *C. R. Geosci.*, *344*, 508–515.

Bonneton, P., J. Van de Loock, J.-P. Parisot, N. Bonneton, A. Sottolichio, G. Detandt, B. Castelle, V. Marieu, and N. Pochon (2011a), On the occurrence of tidal bores—The Garonne River case, *J. Coastal Res.*, *SI 64*, 11,462–11,466.

Bonneton, P., J.-P. Parisot, N. Bonneton, A. Sottolichio, B. Castelle, V. Marieu, N. Pochon, and J. Van de Loock (2011b), Large amplitude undular tidal bore propagation in the Garonne River, France, paper presented at the 21st ISOPE Conference. [Available at http://www.isope.org/publications/proceedings/ISOPE/ISOPE%202011/data/papers/11TPC-1026Bonne.pdf.]

Bonneton, P., E. Barthelemy, F. Chazel, R. Cienfuegos, D. Lannes, F. Marche, and M. Tissier (2011c), Recent advances in SerreGreen Naghdi modelling for wave transformation, breaking and runup processes, *Eur. J. Mech. B Fluids*, *30*(6), 589–597.

Cai, H., H. H. Savenije, and M. Toffolon (2012), A new analytical framework for assessing the effect of sea-level rise and dredging on tidal damping in estuaries, *J. Geophys. Res.*, *117*, C09023, doi:10.1029/2012JC008000.

Chanson, H. (2009), Current knowledge in hydraulic jumps and related phenomena. A survey of experimental results, *Eur. J. Mech. B Fluids*, *28*(2), 191–210.

Chanson, H. (2012), *Tidal Bores, Aegir, Eagre, Mascaret, Pororoca: Theory and Observations*, World Sci., Singapore.

Chanson, H., D. Reungoat, B. Simon and P. Lubin (2011), High-frequency turbulence and suspended sediment concentration measurements in the Garonne River tidal bore, *Estuarine Coastal Shelf Sci.*, *95*(2), 298–306.

Chugh, R. S. (1961), Tides in Hooghly River, *Hydrol. Sci. J.*, *6*(2), 10–26.

Davies, G., and C. D. Woodroffe (2010), Tidal estuary width convergence: Theory and form in North Australian estuaries, *Earth Surf. Processes Landforms*, *35*, 737–749, doi:10.1002/esp.1864.

El, G. A., R. H. Grimshaw, and N. F. Smyth (2006), Unsteady undular bores in fully nonlinear shallow-water theory, *Phys. Fluids*, *18*(2), 027104.

Favre, H. (1935), *Etude Théorique et Expérimentale des Ondes de Translation Dans les Canaux Dcouverts*, Dunod, Paris.

Friedrichs, C. T. (2010), Barotropic tides in channelized estuaries, in *Contemporary Issues in Estuarine Physics*, pp. 27–61, Cambridge Univ. Press, Cambridge, U. K.

Friedrichs, C. T., and D. G. Aubrey (1994), Tidal propagation in strongly convergent channels, *J. Geophys. Res.*, *99*(C2), 3321–3336, doi: 10.1029/93JC03219.

Furgerot, L., D. Mouaze, B. Tessier, L. Perez, and S. Haquin (2013), Suspended sediment concentration in relation to the passage of a tidal bore (See River estuary, Mont Saint Michel Bay, NW France), in *Proceedings of Coastal Dynamics* 2013, edited by P. Bonneton and T. Garlan, pp. 671–682. [Available at http://www.coastaldynamics2013.fr/pdf_files/061_Furgerot_Lucille.pdf.]

Graas, S. and H. H. G. Savenije (2008), Salt intrusion in the Pungue estuary, Mozambique: Effect of sand banks as a natural temporary salt intrusion barrier, *J. Hydrol. Earth Syst. Sci. Discuss.*, *5*, 2523–2542.

Green, A. E., and P. M. Naghdi (1976), A derivation of equations for wave propagation in water of variable depth, *J. Fluid Mech.*, *78*(2), 237–246.

Horrevoets, A. C., H. H. G. Savenije, J. N. Schuurman and S. Graas (2004), The influence of river discharge on tidal damping in alluvial estuaries, *J. Hydrol.*, *294*(4), 213–228.

Lannes, D., and P. Bonneton (2009), Derivation of asymptotic two-dimensional time-dependent equations for surface water wave propagation, *Phys. Fluids*, *21*(1), 016601, doi:10.1063/1.3053183.

Lanzoni, S., and G. Seminara (1998), On tide propagation in convergent estuaries, *J. Geophys. Res.*, *103*(C13), 30,793–30,812, doi:10.1029/1998JC900015.

LeBlond, P. H. (1978), On tidal propagation in shallow rivers, *J. Geophys. Res.*, *83*(C9), 4717–4721, doi:10.1029/JC083iC09p04717.

Lemoine, R. (1948), Sur les ondes positives de translation dans les canaux et sur le ressaut ondulé de faible amplitude, *La Houille Blanche*, *2*, 183–185.

Lynch, D. K. (1982), Tidal bores, *Sci. Am.*, *247*, 146–156.

Madsen, P. A., H. J. Simonsen, and C. H. Pan (2005), Numerical simulation of tidal bores and hydraulic jumps, *Coastal Eng.*, *52*(5), 409–433.

Madsen, P. A., D. R. Fuhrman, and H. A. Schaffer (2008), On the solitary wave paradigm for tsunamis, *J. Geophys. Res.*, *113*, C12012, doi: 10.1029/2008JC004932.

Pan, C., and H. Lu (2011), 2D numercial simulation of tidal bore on Qiantang River using KFVS scheme, *Coastal Eng. Proc.*, *1*(32), pp. 1–13, doi:10.9753/icce.v32.currents.29. [Available at https://icce-ojs-tamu.tdl.org/icce/index.php/icce/article/viewFile/1015/pdf_19.]

Parisot, J.-P., C. Cheng, S. Zaragosi, V. Hanquiez, P. Bonneton, and N. Bonneton (2012), Suivi aérien du mascaret de la Garonne le 10 September 2010, *Géomatique Expert*, *88*, 60–71.

Parker, B. B. (1991), The relative importance of the various nonlinear mechanisms in a wide range of tidal interactions, in *Tidal Hydrodynamics*, edited by B. B. Parker, pp. 237–268, John Wiley, Hoboken, N. J.

Peregrine, D. H. (1966), Calculations of the development of an undular bore, *J. Fluid Mech.*, *25*, 321–330, doi:10.1017/S0022112066001678.

Savenije, H. H. G. (2005), Salinity and Tides in Alluvial Estuaries. Elsevier, N. Y.

Savenije, H. H. G., M. Toffolon, J. Haas and E. J. M. Veling (2008), Analytical description of tidal dynamics in convergent estuaries, *J. Geophys. Res.*, *113*, C10025, doi:10.1029/2007JC004408.

Serre, F. (1953), Contribution à l'étude des écoulements permanents et variables dans les canaux, *La Houille Blanche*, *8*(6), 830–872.

Simpson, J. H., N. R. Fisher, and P. Wiles (2004), Reynolds stress and TKE production in an estuary with a tidal bore, *Estuarine Coastal Shelf Sci.*, *60*(4), 619–627.

Soares Frazao, S., and Y. Zech (2002), Undular bores and secondary waves-Experiments and hybrid finite-volume modelling, *J. Hydraul. Res.*, *40*(1), 33–43.

Tissier, M., P. Bonneton, F. Marche, F. Chazel, and D. Lannes, (2011), Nearshore dynamics of tsunami-like undular bores using a fully nonlinear Boussinesq model, *J. Coastal Res.*, SI *64*, 603–607.

Toffolon, M., G. Vignoli, and M. Tubino, (2006), Relevant parameters and finite amplitude effects in estuarine hydrodynamics, *J. Geophys. Res.*, *111*, C10014, doi:10.1029/2005JC003104.

Treske, A. (1994), Undular bore (*Favre*-waves) in open channels—Experimental studies, *J. Hydraul. Res.*, *32*(3), 355–370.

Uncles, R. J., J. A. Stephens, and D. J. Law (2006), Turbidity maximum in the macrotidal, highly turbid Humber Estuary, UK: Flocs, fluid mud, stationary suspensions and tidal bores, *Estuarine Coastal Shelf Sci.*, *67*, 30–52.

van Rijn, L. C. (2011), Analytical and numerical analysis of tides and salinities in estuaries; part I: Tidal wave propagation in convergent estuaries, *Ocean Dyn.*, *61*(11), 1719–1741.

Vandenbruwaene, W., Y. Plancke, T. Verwaest, and F. Mostaert (2013), *Interestuarine Comparison: Hydrogeomorphology: Hydro- and Geomorphodynamics of the TIDE Estuaries Scheldt, Elbe, Weser and Humber. Version 4. WL Rapporten*, Flanders Hydraul. Res., Antwerp, Belgium.

Wei, G., J. T. Kirby, S. T. Grilli, and R. Subramanya (1995), A fully nonlinear Boussinesq model for surface waves. Part 1. Highly nonlinear unsteady waves, *J. Fluid Mech.*, *294*, 71–92.

Wolanski, E., D. Williams, S. Spagnol and H. Chanson (2004), Undular tidal bore dynamics in the Daly Estuary, Northern Australia, *Estuarine Coastal Shelf Sci.*, *60*(4), 629–636.

Zhang, J., C. Zhang, X. Wu, and Y. Guo (2012), *Astronomical Tide and Typhoon-Induced Storm Surge in Hangzhou Bay, China, Hydrodynamics*, edited by H. E. Schulz, A. L. A. Simoes, and R. J. Lobosco, Hydrodynamics: Natural Water Bodies. InTech, pp. 179–198, doi:10.5772/28153.